Compliant Aortic Annulus Sizing with Different Elliptical Ratios Through a Valvuloplasty Balloon Catheter

Junke Yao, Giorgia Maria Bosi, Andrea Palombi, Gaetano Burriesci, Helge Wurdemann

***Abstract*— *Objective*: Aortic stenos (AS) is a heart valve disease that commonly affects the elderly. Transcatheter aortic valve implantation is a minimally invasive treatment that allows to replace the function of the diseased native valve with a prosthetic device, relying on catheters for device implantation. According to the current clinical guidelines, the choice of the implanted device is based on preoperative sizing determined by image-based technology. However, this assessment faces inherent limitations that can lead to sub-optimal sizing of the prosthesis; in turn, this can cause major post-operative complications like aortic regurgitation or cardiac electrical signal disruption. *Method*: By utilizing balloon pressure and volume data, this paper proposes an intra-operative method for determining the dimension of the aortic annulus which takes into account its compliance and geometric irregularity. The intra-balloon pressure-volume curves were obtained using an Automated Balloon Inflation Device operating a commercially available valvuloplasty balloon catheter. A sizing algorithm to estimate the dimensions of the annulus was integrated via a validated analytical model and a numerical model for balloon free-inflation. Tests were performed on circular and elliptical idealised aortic phantoms. *Results*: Experimental results confirm that the pressure-volume data processed with the sizing algorithm can be used to determine the circular annular diameter for all tissue rigidities. *Conclusion*: The measurement of stiffer elliptical annulus phantoms shows good accuracy and high repeatability. *Significance*: This work represents substantial progress toward improving the selection of TAVI devices by using balloon catheters to improve the sizing of compliant aortic annuli with complex geometry.**

***Index Terms*— Balloon Valvuloplasty Catheters, Balloon Sizing,TAVI, Aortic Stenosis, Aortic Annulus, Balloon Aortic Valvuloplasty**

I. INTRODUCTION

Valvular heart disease (VHD) is a subset of heart disease in which one of four heart valves becomes dysfunctional due to the narrowing of the valve opening (stenosis) or aberrant closure (regurgitation), resulting in restricted blood flow or backflow. More than 2% of the population is diagnosed with VHD, which is associated with increased mortality [1], [2]. The aortic valve is a one-way valve that regulates the blood flow ejected from the left ventricle to the aorta. Aortic stenosis, which manifests as a complex process involving chronic inflammation, lipoprotein deposit, and age-related calcification, results from the aortic valve's aberrant opening of the aorta. In Europe and North America, AS is the most frequent primary valve lesion that requires surgery or transcatheter intervention [3], and its incidence is increasing as the population ages [4]. Although surgical aortic valve replacement (SAVR) is considered as the class I recommended treatment for AS, more than 33% of high-risk and severely symptomatic patients are not eligible to undergo SAVR due to their advanced age, left ventricular failure, or multiple concurrent health conditions [5]–[7]. Since its introduction in 2002, transcatheter aortic valve implantation (TAVI) has supplanted SAVR as a minimally invasive intervention for high-risk patients and those deemed unsuitable for surgery [8]. This treatment relies on the use of balloon catheters, either for prosthetic valve implantation or as a bridge to TAVI for pre-dilatation or post-dilatation, as with balloon aortic valvuloplasty (BAV). Correct sizing of the prosthetic device is crucial due to its association with intra-operative complications, including paravalvular regurgitation and aortic annulus rupture [9]. Malpositioning or undersizing of the implantation device, the elliptic annulus anatomy, or irregular distribution of the calcification on leaflets are the main causes of regurgitation [9], [10]. On the other hand, an oversized prosthesis can result in damage to the host tissues and cause atrioventricular block.

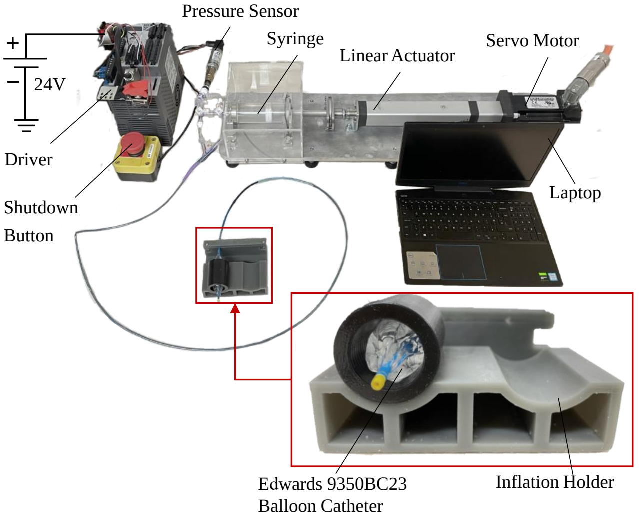

Fig. 1. Experimental setup for sizing and measuring idealised aortic annular compliant phantoms.

Two-dimensional imaging techniques based on transthoracic echocardiography (TTE) or transesophageal echocardiography (TEE) are the imaging modality of choice for the size assessment [11]. Most commonly, the measured diameter is the distance between the hinge points of the aortic valve leaflets at the end of systole, when the annular diameter is at its maximum. However, a significant underestimation of diameter, especially for irregular annulus, results through TTE and TEE because these 2D imaging techniques lack Three-dimensional (3D) information [12]–[15]. 3D techniques based on multi-detector computed tomography (MDCT), 3D transesophageal echocardiography (3D-TEE), and cardiovascular magnetic resonance (CMR) are well researched. Although studies have shown that MDCT reduces the incidence of regurgitation [15], this approach increases the risk of contrast nephropathy in patients with renal morbidity, especially in elderly AS patients [16]. 3D-TEE and CMR have emerged as potential alternative, provide three-dimensional information without contrast administration and radiation [17]. However, these imaging

Junke Yao, Giorgia Maria Bosi, Gaetano Burriesci, and Helge Wurdemann are with Faculty of Engineering Science, Mechanical Engineering, University College London, Gower Street, London, UK (e-mail: junke.yao.19@ucl.ac.uk).

Andrea Palombi (e-mail: andrea.palombi.16@ucl.ac.uk).

Gaetano Burriesci is the group leader of Bioengineering at Ri.MED Foundation, Palermo, Italy (e-mail: g.burriesci@ucl.ac.uk).

modalities are not widely available due to their high cost and time-consuming nature [18]. In addition, patients with pacemaker are suitable for MR imaging, and MRI-conditional pacing leads and boxes are only allowed to be scanned at 1.5T field strength [19].

Preoperative imaging techniques have two inherent limitations. Firstly, the measurements are frequently manually processed and subjectively reliant on the operator judgement and experience. Secondly, the optimum instant in the cardiac cycle for the evaluations is still a topic of contention [20], [21]. In addition, the potential changes in the annular geometry caused by BAV are not taken into account.

Intraoperative sizing techniques can detect annular dimensions after the diseased valve enlargement and balloon dilatation simultaneously, whereas such dimension changes cannot be determined through pre-operative approaches. Intraoperative assessments based on BAV balloon catheters were proposed in several studies to overcome the drawbacks of sizing done via imaging techniques [22]–[25]. These can be used to validate or reject the size of the prosthesis chosen during preoperative assessment, but they cannot offer an accurate measurement of the annular diameter. In these studies, the same injected volume or internal balloon pressure as during the dilatation is used to inflate a new balloon catheter *in vitro*. However, the real balloon inflated diameter would change when freely inflated and when within the valve, which might lead to the error of the measurement. As a result, the information provided during the operation for the prosthesis valve selection is limited with respect to annulus tissue and geometry.

In this paper, we propose an intra-operative method for determining the aortic annular diameter based on its compliance and elliptical geometry properties while using intra-balloon pressure-volume (*p*-*v*) data obtained from a robotised aortic valvuloplasty balloon catheter. An automatic balloon inflation device was designed and connected to a balloon catheter to collect the real-time pressure data and control the volume and inflation speed. The configuration of the annular phantoms ranges from simple to complex: circular, elliptical and 3D models of standard aortic roots are used to investigate the performance of the method on clinically realistic geometries. The annular diameters of phantoms were estimated through a sizing algorithm by *p*-*v* data that was obtained in experimental tests (Fig. 1) on compliant aortic phantoms of different shore hardness.

II. MATERIALS AND METHODS

This section explains the working principle of the motorised inflation device with a pressure sensor to control and monitor the BAV balloon catheter during *in vitro* valvuloplasty. Furthermore, the data from the pressure transducer is fed into estimation algorithms to find the diameter and compliance property.

When the balloon is inflated to its nominal internal volume during the balloon catheter dilatation procedure, its membrane is stretched. The internal pressure of the balloon increases as a result of stretching, and a balloon model that takes into account the relationship between internal pressure and volume to determine the diameter of the balloon can be determined. The changing internal pressure-volume curve and the free inflation curve are compared after the balloon has been inflated inside an annulus. The diameter of the balloon when the annulus begins to expand will be approximated based on the results comparison. The method used to perform the comparison, as well as the estimation approach, are explained in this section after the section describing the experiment.

A. The compliant phantoms

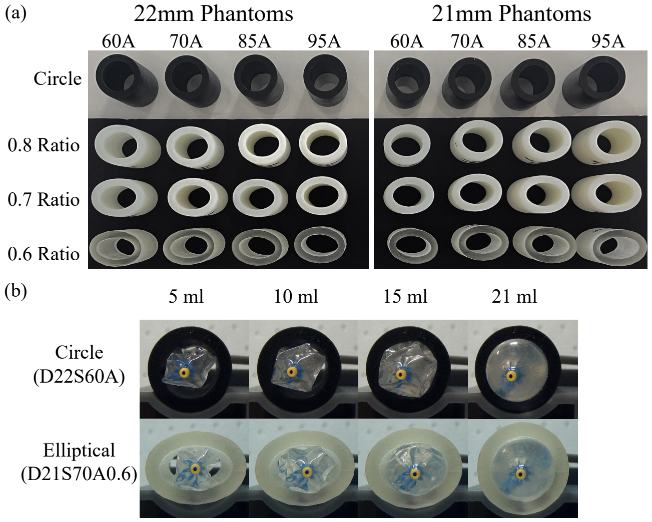

Fig. 2. (a) Phantoms of 21 and 22 mm in circular and 0.6, 0.7, and 0.8 elliptical ratios; (b) The front views of the balloon inflated inside a 22 mm circular phantom with 60A shore hardness and a 21 mm 0.6 elliptical phantom with 70A shore hardness.

TABLE I

DIMENSIONS OF ELLIPTICAL ANNULAR PHANTOMS

Circumference/ Diameter (mm)		Elliptic Rates 0.6	0.7	0.8
65.97/ 21	LD*/ SD* (mm)	25.85/ 15.51	24.52/ 17.16	23.26/ 18.61
69.12/ 22	LD/ SD (mm)	27.08/ 16.25	25.68/ 17.98	24.37/ 19.50

*LD: long diameter; SD: short diameter.

The set of compliant circular annular phantoms consisting of eight cylinders was fabricated by 3D printing with PolyJet technology, Objet500 Connex (Stratasys Inc., Rehovot, Israel). Inner diameters of 21 and 22 mm were created for sizing, with 5 mm in thickness, and 40 mm in length. A Young's modulus in the range of 13.4 to 31.8 MPa is reported for calcified aortic valve tissue in patients with symptomatic severe aortic stenosis [26]. A relationship between the elastic modulus and the shore hardness was developed by Qi *et al.* [27] and used in research by Guarnera *et al.* for atherosclerotic plaque reconstructions [28]. Based on this calculation, the calcified annulus has a shore hardness range from 75A to 91A. This range was expanded to encompass 60A, 70A, 85A, and 95A, in order to take into account aortic valve under moderate aortic stenosis. Compliance was adjusted through the combination of two different curable liquid photopolymers: Tango Black Plus (a rubber-like material) and VeroClear (a rigid and robust material). The shore hardness value becomes larger based on the percentage of VeroClear, with 95A representing the most rigid material in the phantoms tested.

In order to take into account the effect of the irregularity of the annulus, elliptical phantoms were created based on clinical data. In particular, the annuli are commonly classified as elliptical (non-circular) when the ratio between the shortest and longer diameters becomes lower than 0.82 [29], and the literature reports extremely low ratios measured from imaging of about 0.6 [30]. Hence, three elliptic ratios 0.6, 0.7, and 0.8 were considered for the phantoms, covering the 'circular range' (ratios 1.0 - 0.8), common ellipticities (ratios 0.8 - 0.7) and extreme ellipticities (ratios 0.7 - 0.6). Since the use of circumference-derived diameter by 3D TEE is reported to result in a lower incidence of paravalvular aortic regurgitation [31], the elliptical sets were built with inner perimeters equal to the circumferences of 21

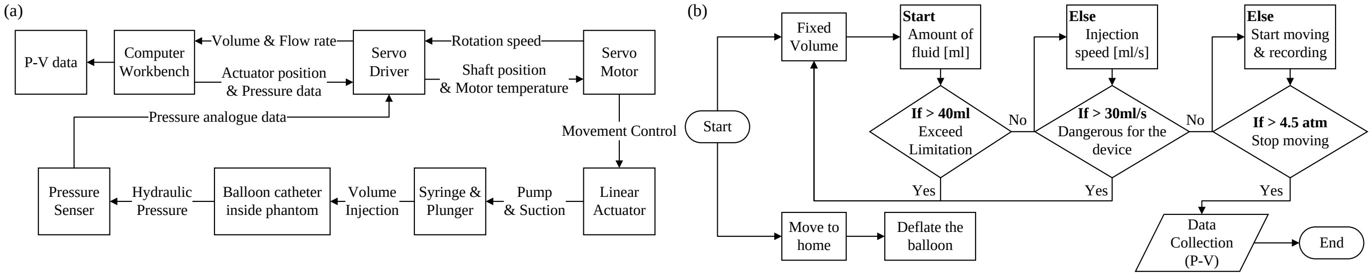

Fig. 3. (a) The workflow of the experimental setup to get *p-v* data without rupturing the balloon; (b) The ABID workflow with two alternative options implemented on the Workbench computer interface, where *p-v* represents Pressure-Volume data. When the input volume and speed exceed the limiting value, the system returns to the first step for new input values within the constraint. After reading the appropriate inputs, the balloon is inflated until the internal pressure exceeds 4.5 atm.

and 22 mm, and the same four shore hardness ratings. The elliptical phantoms were made of Agilus 30 (a highly flexible photopolymer) and VeroClear (a rigid photopolymer), using a wall thickness and axial length identical to the circular phantoms.

The 32 resulting annular phantoms (8 circular and 24 elliptical) are represented in Fig. 2(a), with the dimensions of the elliptical configurations summarised in Table I.

B. The automated balloon inflation device

An Automated Balloon Inflation Device (ABID) was built and utilised to inflate the balloon catheter with a specific speed and volume, as shown in Fig. 1. A 50 ml gas-tight syringe from ILS (Stuetzerbach, Germany) is fixed on a 15 mm thick plate (AISI 304 stainless steel), where a Luer-lock connector, metal collar, and seals are equipped for leakage protection. The syringe is enclosed in a transparent box to ensure safety of the operator. The movement of the plunger is regulated by a Kollmorgen AKM22G-ANDNC-00 Servo motor (Altra Industrial Motion, Braintree, MA, USA) and coupled with a Thomson ball screw linear actuator (PC25LX999B03-0100FM, Thomson, Kristianstad, Sweden). To avoid the balloon being inflated beyond the burst pressure, pressure data is acquired using a PXM319-007A10V pressure transducer (Omega Engineering Inc., Stamford, CT, USA) to stop the actuator once the intra-balloon pressure reaches the burst pressure declared by the manufacturer. A Kollmorgen AKD-T00606 BASIC drive with expanded I\O controls the system and optimises the performance via a computer interface. The signal workflow is shown in Fig. 3(a). The desired volume and injection speed of the syringe is sent to the servo driver, which converts the values into rotation speed, allowing the servo motor to control the linear actuator that pushes the syringe's plunger. During the inflation, the hydraulic pressure inside the balloon is recorded by the pressure transducer and the actuator real-time position is translated into the injected volume and saved as *p-v* data.

ABID is entirely managed by AKD Workbench software, which provides the coding interface based on the AKD BASIC programming language to control the inflation/deflation and the amount of fluid to be injected or withdrawn. There are two options to control the ABID, as shown in Fig. 3(b). Option "Fixed volume" allows the balloon catheter to be inflated with a user-defined volume and injection speed, whereas Option "Move to home" deflates the balloon using a user-defined rate. The injection amount and speed are restricted during balloon inflation for safety and to avoid rupture of the balloon. A pressure transducer measures the internal pressure, and the actuator motion is arrested when the pressure reaches 4.5 atm.

C. Experimental setup and test protocol

To validate the proposed sizing and measuring approaches, a balloon catheter is inserted into the sets of compliant aortic annular phantoms. Two diameters, 21 mm and 22 mm, are used, which are compatible with the balloon. This is fully deployed to its maximum diameter 23 mm. The length of the phantoms is 40 mm, which covers the cylindrical region of the balloon and avoids the formation of a waist during balloon inflation. The balloon catheter is connected to the syringe, which is driven by a linear actuator controlled by a servo motor. The signal workflow is shown in Fig. 3(a); the pressure transducer records the pressure.

The protocol is as follows:

1) The syringe, the pressure sensor on ABID, and the catheter are filled with a saline solution, and the balloon is inflated with a small amount of solution to keep the internal balloon pressure at one atmosphere.
2) The deflated balloon is placed horizontally inside the phantom, with no constraint on the two sides of the balloon.
3) A volume of 21 ml and a flow rate of 1 ml/s are inputted to the AKD interface to control the syringe.
4) The balloon is inflated until the absolute intra-balloon pressure reaches 4.5 atm.
5) A one-minute duration between each test is imposed to minimise the impact of viscoelastic effects.

The balloon inserted inside the phantoms with different inflated levels is shown in Fig. 2(b), where the phantom was placed on a holder and the 21 mm circular phantom started to be expanded between 15 and 21 ml and the 21 mm elliptical phantom with ratio 0.6 starts to be deformed between 10 and 15 ml while the balloon membrane is not stretched. Five tests were performed for each phantom, and the acquired *p-v* curves were imported into Matlab and processed by the estimation algorithm.

D. Balloon analytical model

High-pressure balloon catheters that apply force and which are designed to inflate to a defined diameter are widely used in medical procedures like angioplasty and valvuloplasty. A commercially available valvuloplasty balloon catheter (Edwards Lifesciences, Irvine, USA) was selected as an experimental device. The diameter of the balloon with a volume of 21 ml is 23 mm at an internal gauge pressure of 4 atm ($\simeq$ 0.4 MPa). The inflation procedure was divided into two phases: unfolding and stretching. When deploying the balloon inside the elliptical phantoms, the balloon might not be completely unfolded when starting the stretching phase when reaching phantoms' minor/short diameter. Thus, the unfolding stage needs to be represented by an analytical model. To simplify the complex unfolding procedure, the first phase was converted into a linear elastic expansion of the balloon model with different material parameters, representing the unfolding inflation under very low pressures [32]. Therefore, the analytical models of the balloon during the two phases had the same configuration. They were modelled as a pressurised, cylindrical thin-walled vessel with two hemispherical ends. The longitudinal cross-section illustration shown in Fig. 4(a) was used for phantom sizing before the balloon caused the phantom to expand.

The radial stress through the balloon wall is insignificant when the thickness to inner diameter ratio is less than 1/20, and the circumferential and axial stress may be approximated as evenly distributed throughout the wall for the closed thin-walled cylinder. The balloon membrane is modelled as a linear elastic and isotropic material. A 'virtual' Young's modulus during the unfolding phase was determined by the stress and strain [32] as (1) and (2) to (3), where D_0 is the folding diameter of the balloon, D_u is the unstretched diameter of the balloon, t_c is the thickness of the cylinder part, and p_i is the internal pressure. When the balloon reaches an unstretched diameter, the internal pressure is still one atmosphere (0.1 MPa). According to the circumference of the unstretched balloon deflated into a folded star-shape with six edges, the folded diameter is roughly assigned as the length of one edge. Therefore, the folding diameter is 10.88 mm and the 'virtual' Young's modulus is 22.81 MPa with the 0.5 mm thickness of the balloon.

$$\sigma_{unfold} = \frac{p_i D_u}{2t_c} \tag{1}$$

$$\varepsilon_{unfold} = \frac{D_u - D_0}{D_0} \tag{2}$$

$$E_{unfold} = \frac{p_i D_u D_0}{2t_c(D_u - D_0)} \tag{3}$$

The volumetric strains of the balloon model can be written, as (4) and (5) where p_i is the internal pressure, p_e is the external pressure, D is the initial diameter of the balloon (D_0 for the unfolding model and D_u for stretching model), t_c is the thickness of the cylinder part, t_s is the thickness of the hemispherical portions, and E and ν are the Young's modulus and the Poisson's ratio of the balloon material, respectively.~~.~~

$$\varepsilon_c = \frac{(p_i - p_e)D}{4t_c E}(5 - 4\nu) \tag{4}$$

$$\varepsilon_s = \frac{3(p_i - p_e)D}{4t_s E}(1 - \nu) \tag{5}$$

$$V(p) = \frac{\pi L D^2}{4}(1 + \varepsilon_c) + \frac{\pi D^3}{6}(1 + \varepsilon_s) \pm c \tag{6}$$

The volumetric strains are used for defining the instantaneous balloon volumetric variation by the difference of the internal and external pressure during free inflation as (6), where L is the unstretched length of the cylindrical region. The absolute value of c is a constant residual volume when the balloon is deflated to keep the internal pressure as one atmosphere using ABID. The initial volume of the unfolding model lacks the residual volume of the stretching model, so the former $V(p)$ equation adds c while the latter one subtracts c. The values of E and ν (556 MPa and 0.45) for the stretching phase were experimentally determined by tensile tests, and the other parameters were obtained in our previous study, as shown in Table II. c and t_s are calculated by fitting the free inflation pressure-volume (p-v) curve through ABID with a root-mean-square error (RMSE) equal to 0.10 (R^2 = 0.9), as demonstrated by the pink plot in Fig. 5(a).

The diameter calculated according to the transmural pressure of the balloon membrane is shown in Equation 7, where D_e is the estimated diameter.

$$D_e = D + \frac{(p_i - p_e)D^2}{4t_c E}(2 - \nu) \tag{7}$$

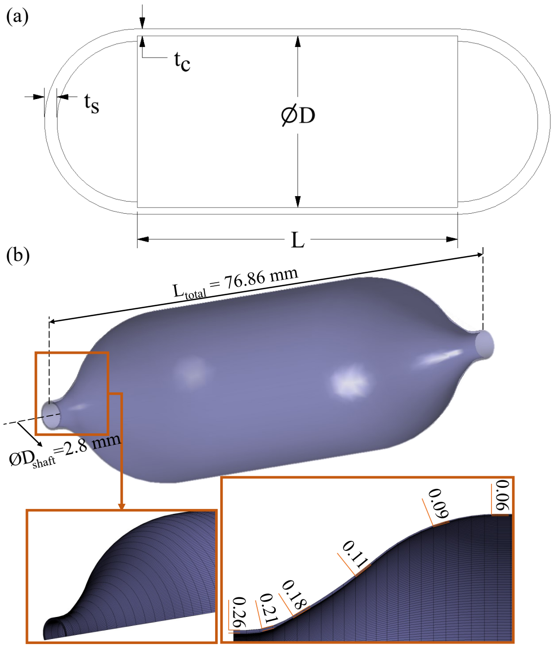

Fig. 4. Models of a commercially available balloon catheter. (a) The cross-section of the balloon analytical model; (b) The numerical model of the balloon with the measured thickness of the device.

TABLE II
PARAMETERS FOR BALLOON ANALYTICAL MODEL

Parameters	D_0 /mm	D_u /mm	L /mm	t_c /mm	t_s /mm	c /mm^3	p_i /atm
Values	10.88	20.75	35.82	0.05	0.05	3440	1.00

E. Balloon numerical model

To model the process more accurately, a numerical model was developed with tapered ends and the thickness measured from an actual device, as shown in Fig. 4(b). The measurements were recorded from a polariscopic image, and a reconstruction of the non-collapsed geometry of the unstretched balloon was imported into Solidworks (Dassault Systèmes, Vélizy-Villacoublay, France). The material model of the balloon was assumed to be isotropic linear elastic, with a Poisson's ratio of 0.45 and a Young's modulus of 556 MPa according to the linear regression performed on the stress-strain curve from the experimental uniaxial tensile test [33].

1) Simulation: Hypermesh 2019 (Altair Engineering Inc., Troy, Michigan, USA) was used to mesh the balloon model, which was discretised with 8-node hexahedral solid elements (46800, after independent sensitivity test). The inflation simulation was performed with ANSYS v19.0 (ANSYS Inc., Canonsburg, USA), choosing the implicit method with large deformation. A transmural pressure linearly increasing from zero to 4 atm over 3 seconds was applied to the balloon's membrane. The balloon volume at each step was measured by ANSYS SpaceClaim (ANSYS Inc., Canonsburg, USA), resulting in the numerical p-v data at the end of the simulation.

2) Data processing: The diameter of the balloon at the different applied pressures was measured as the average displacement of a set of nodes located on the centre circle of the balloon cylindrical part, recorded as diameter-pressure (D-p) data. The analytical model of the volume function through internal pressure is monotonically linear, and the estimated diameter equation expressed by the pressure is quadratic. Therefore, the p-v and D-p datasets were fitted with a linear line and a second polynomial, respectively, expressing the transmural pressure as a function of the volume, with an additional parameter c_n for x-axis shifting as the remaining volume. The diameter as a function of the pressure based on the unstretched diameter (20.75 mm) is then used in (8) and (9). All parameters are shown in Table III, which results in an RMSE with the free inflation *p-v* data via ABID equal to 0.13 (R^2 = 0.87), as shown in the green plot in Fig. 5(a).

The unfolding phase was also considered for the numerical model. A volume-diameter $V-d$ curve was obtained by simulating the inflation of a tri-folded deflated balloon model to its nominal internal volume (21 ml) in one of our previous studies, since the internal pressure would remain at one atmosphere. A third polynomial was used to fit the $V-D$ curve data as (10), with the parameters shown in Table IV; c_u was also used for x-axis shifting in terms of residual volume. Therefore, when the estimated diameter is less than the unstretched diameter, the $V-d$ curve is used to calculate the diameter by the volume reaching the contact point.

$$p(V) = a(V + c_n) + b \tag{8}$$

$$D_{stretch}(p) = dp^2 + ep + 20.75 \tag{9}$$

TABLE III
PARAMETERS FOR BALLOON NUMERICAL MODEL

Parameters	a	b	c_n	d	e
Values	1.13	-18.90	3.40	0.05	0.45

$$D_{unfold}(V) = f(V + c_u)^3 + g(V + c_u)^2 + h(V + c_u) + j \tag{10}$$

TABLE IV
PARAMETERS FOR BALLOON NUMERICAL UNFOLDING MODEL

Parameters	f	g	h	j	c_u
Values	0.0055	-0.23	3.41	2.54	2.16

F. Diameter estimation algorithm

Balloon inflation inside a compliant ideal circular aortic annulus phantom has three states: 1) no-tension inflation; 2) tensioned inflation; 3) phantom expansion. The inter-balloon pressure remains static before the balloon reaches the unstretched diameter of the first state. For the second state, the pressure starts to increase by stretching the balloon until it is in complete contact with the phantom. When the balloon is in full contact with the annulus, the latter deforms by increasing its diameter, with the pressure increment slope influenced by the compliance of the phantom. The sizing approach is based on the assumption that the diameter of the balloon is equal to the annular diameter without annulus deformation at the time when complete contact is almost reached. Thus, sizing for the circular compliant annulus can be performed indirectly by identifying the point within the acquired data at which the pressure increment deviates from the free inflation curve and estimating the corresponding balloon diameter according to *D-p* functions obtained from balloon models.

However, when the balloon is inflated inside a compliant elliptical aortic annulus phantom, the contact situation is too complex to be divided into several states. The short diameter of the phantom is lower than the unstretched diameter of the balloon. Therefore, the contact point is not located on the free inflation curve, and the pressure starts to increase at a lower injected volume. Therefore, sizing for the minor diameter of the elliptical compliant annulus can be achieved indirectly by determining the volume inside the balloon when the pressure increases from one atmosphere, as the balloon begins to touch the narrow wall of the elliptical phantom. Unfolded balloon models with their *D-p* functions are utilised for estimating the short diameter of the elliptical phantoms. In addition, when the elliptical ratio is close to 1 (e.g. 0.8), the balloon might expand the phantom to a circle without considerable phantom expansion stress. Thus, the equivalent diameter of the elliptical phantom with a 0.8 ratio can be assessed similarly to circular phantoms.

Algorithm 1: Compliant phantom sizing estimation

```
Input: Experimental p-v Data
Output: Estimated Diameters
Get Smoothed $1^{st}$ and $2^{nd}$ Derivative of p-v Data;
Record the maximum peaks of $2^{nd}$ Derivative;
Record other two peaks on the two sides of Max if present;
Define finalPeaks as list of recorded peaks;
Delete zero element in finalPeaks;
peakNumber = size(finalPeaks);
switch peakNumber do
    case 1 do
        Extract p-v Data from indexMax to end;
    end
    case 2 do
        if indexMax == finalPeaks(1) then
            Extract p-v Data from indexMax to indexThird;
        else
            Extract p-v Data from indexMax to end;
        end
    end
    case 3 do
        Extract p-v Data from indexMax to indexThird;
    end
end
inflatePoint = findPeaks(1);
Fit extracted p-v Data with a Line;
while $RMSE < setRMSE$ do
    Delete First Data point;
    Fit Updated p-v Data with a Line;
    Calculate RMSE;
end
Solve the Interaction $\begin{cases} Fitted\ Line \\ Model\ V(p)\ Line \end{cases}$ for getting $p$;
Substitute $p$ in $\begin{cases} Eq.\ (7) - Analytical \\ Eq.\ (9) - Numerical \end{cases}$ for getting $D(1)$;
Solve the Interaction $\begin{cases} Fitted\ Line \\ Pressure = 1\ atm \end{cases}$ for getting $V$;
Substitute $V$ in $\begin{cases} Unfold\ Eq.\ (6)\ to\ get \\ p\ for\ Unfold\ Eq.\ (7) \\ \\ Eq.\ (10) - Numerical \end{cases}$ for getting $D(2)$;
return Diameter list: D
```

The diameter of annular phantoms are estimated by importing pressure-volume data into MATLAB (MathWorks, Natick, USA), which is followed by the data processing. For the circular annulus, linear regression is applied to the region between the start of the second state and the start of the third state, which is extracted from the *p-v* dataset. To extract the region, the *p-v* data and its second numerical derivative are processed by a robust local regression (RLOESS) and a locally weighted regression (LOWESS) filters with smoothing firstly. Then smoothed data is utilised to find the beginning

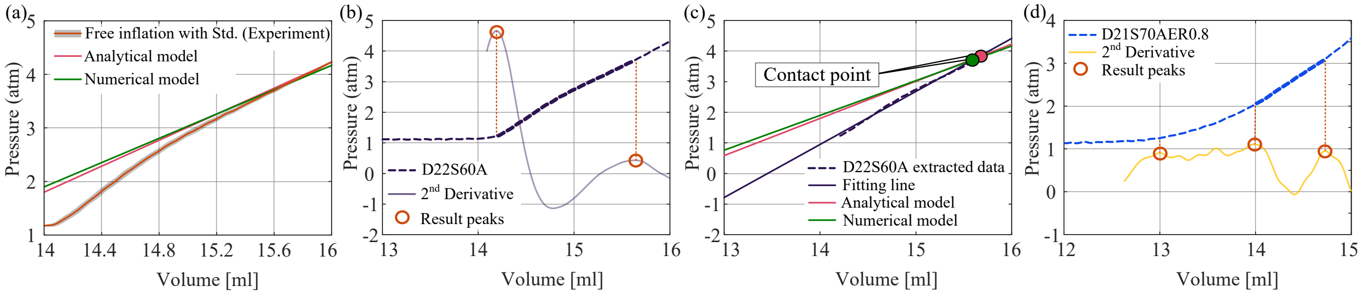

Fig. 5. Model inflation curves and data extraction: (a) The analytical and numerical model curves and the average free inflation data with its standard deviation; (b) The experimental $p-v$ data of balloon inside a 22 mm diameter phantom with shore hardness 60A, where the start (left orange circle) of the second state and its end (right orange circle); (c) The linear regression of the extracted data causes intersections (pink and green points) with the analytical and numerical model lines; (d) The experimental $p-v$ data for an elliptical phantom (70A, 0.8 ratio and 21 mm), and three orange circles are the second derivative peaks for the short and equivalent diameter estimation, where the first orange circle is used for the short diameter, and the thicker dashed line region between the latter two orange circles is used for the equivalent diameter.

of the second and third states. For the beginning of the second state, the internal pressure of the balloon changes from one atmosphere to a higher value within a short time, which results in the maximum value of the second derivative. Therefore, according to the second derivative, the data before its maximum value can be regarded as the first state, and the point at the maximum is recorded (the first orange circle in Fig. 5(b)). Another peak is searched after the maximum second derivative peak as the start of the third state (the second orange circle in Fig. 5(b)) if it is founded. When two peaks are recorded, data between these two points is extracted (the thicker dashed line in Fig. 5(b)). If only the maximum peak is recorded, data after the point is extracted. The resulting *p*-*v* data is updated by deleting the lowest data point until the fitting line via linear regression shows the associated RMSE lower than an empirically set threshold (0.03). The intersections of the analytical model *p*-*v* line and numerical model *p*-*v* line with the resulting linear regression is obtained, such as the green and pink points in Fig. 5(c), to get pressure values at that point for calculating the diameters via *D*-*p* functions of two models.

The short diameter of an elliptical annular phantom is estimated by detecting the volume when the pressure deviates from one atmosphere. The peaks of the smoothed second numerical derivative is recorded because the pressure shows an abrupt increase. The maximum peak of the second derivative is recorded first, and peaks before and after are then recorded. The first peak is assigned as the contact point, and the volume value at that point is recorded. The volume is introduced to the unfolded analytical model *p*-*v* line to determine the pressure for calculating the estimated short diameter by solving the *D*-*p* function. For the numerical model, the minor diameter is assessed directly by solving the V-D function. The equivalent diameter of the elliptical annulus with 0.8 ratio is also estimated by linear regression between the data of the maximum peak and the possible peak of the second derivative, as shown in Fig. 5(d). When phantoms with an elliptical ratio are lower than 0.8, their equivalent diameters are impractical to assess since the phantoms expand to the same shape as the balloon with large deformation. Algorithm 1 shows the simplified sizing estimation procedure.

III. RESULTS

The unique *p*-*v* curves with associated standard deviation values for each phantom are obtained by averaging the results of five tests with different elliptical ratios (Fig. 6). The slope of the portion of the *p*-*v* curve deviating from one atmosphere increases with the stiffness of the phantom with the same annular diameter. In comparison, the volume of the point varying from one atmosphere decreases with the elliptical ratio. In addition, the slope increases with the elliptical ratio of the phantom with the same circumference and shore hardness. For circular phantoms, the parts of the *p*-*v* curves during the pressure increase of 21 mm phantoms are nearly parallel with the portions of the curve deviating from the previous slope after the pressure increase of 22 mm phantoms. When the elliptical ratio is 0.6, the *p*-*v* curves show multiple slope regions more clearly, especially for phantoms with a shore hardness of 60A or 70A, where instead of abrupt increase as free inflation, pressure increases slowly at first within around 2 ml volume ejection, followed by the high slope.

To estimate the circular annulus of 21 mm diameter phantoms, fitting lines for the extracted data with different shore hardness get intersection points with the analytical model and numerical model lines when the balloon touches the phantom and the pressure increment deviates from the free inflation; one of the five tests for each circular phantom is shown in Fig. 7(a). The pressure values of the pink and green points are used to calculate the estimated diameter of phantoms according to the analytical and numerical models. In addition, the pressure of the numerical intersection has a higher value than that of the analytical intersection for all shore hardness levels. The analytical average estimated diameters for circular phantoms are 21.20, 21.03, 21.00 and 20.8 mm for 60A to 95A shore hardness, resulting in an error of 0.94%, 0.15%, 0.02% and 0.71%, respectively. The average estimated diameters by the numerical model for the same phantoms are 21.31, 21.11, 21.05 and 20.92 mm for four material hardness, resulting in an error of 1.49%, 0.54%, 0.24% and 0.36%, as shown in Fig. 7(b). The 85A hardness phantom has the best estimation results in both models, and the estimated value decreases with the stiffness increase. The maximum standard deviation for estimating the 21 mm circular phantoms by two models is ±0.19 mm.

Elliptical phantoms with the same circumference and a 0.8 ratio have an estimated equivalent diameter performance with the lowest error (0.094%) at 60A shore hardness via the analytical model. The best estimation for the numerical model is at 70A with an error of 0.16%. The maximum standard deviation is ±0.47 mm. All results show an estimated diameter value between 21.25 to 20.00 mm with errors lower than 5% in Fig. 7(c) and Fig. 9(a). Regarding the short diameter estimation in elliptical phantoms of the same perimeter (Fig. 7(d)-(f)), the average estimated results of phantoms with 60A and 70A shore hardness are between 18 and 19 mm. When estimating the 0.8 elliptical phantoms, the minor diameter has the smallest error at 1.39% for analytical and 1.24% for a numerical model for 60A phantoms. For a 0.6 ratio, the two softer phantoms have assessed average diameters of 18.42 (error = 18.79%) and 18.11 (error = 16.78%) mm for the analytical model and 19.22 (error = 19.22%) and 18.29 (error = 17.98%) mm for the numerical model in Fig. 9(b),

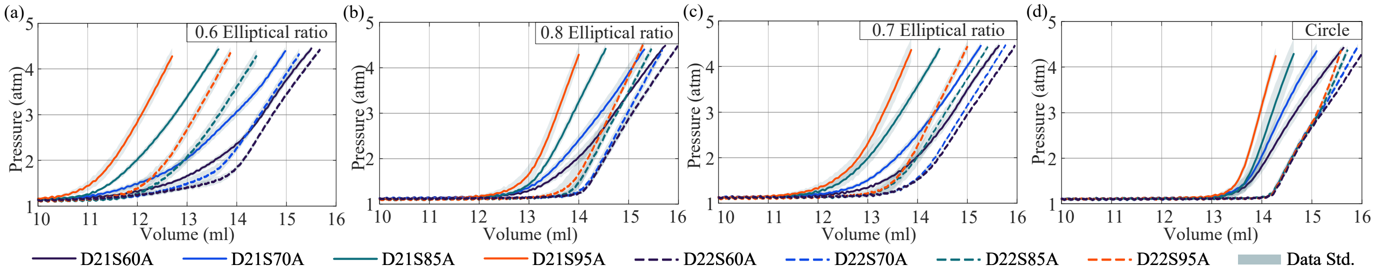

Fig. 6. The average *p*-*v* curves with their standard deviation drawn as a shadow, sorted by the elliptical ratio or circle, where the lines are phantoms having a circumference of 21 mm diameter circle and the dash lines are that of 22 mm diameter circle.

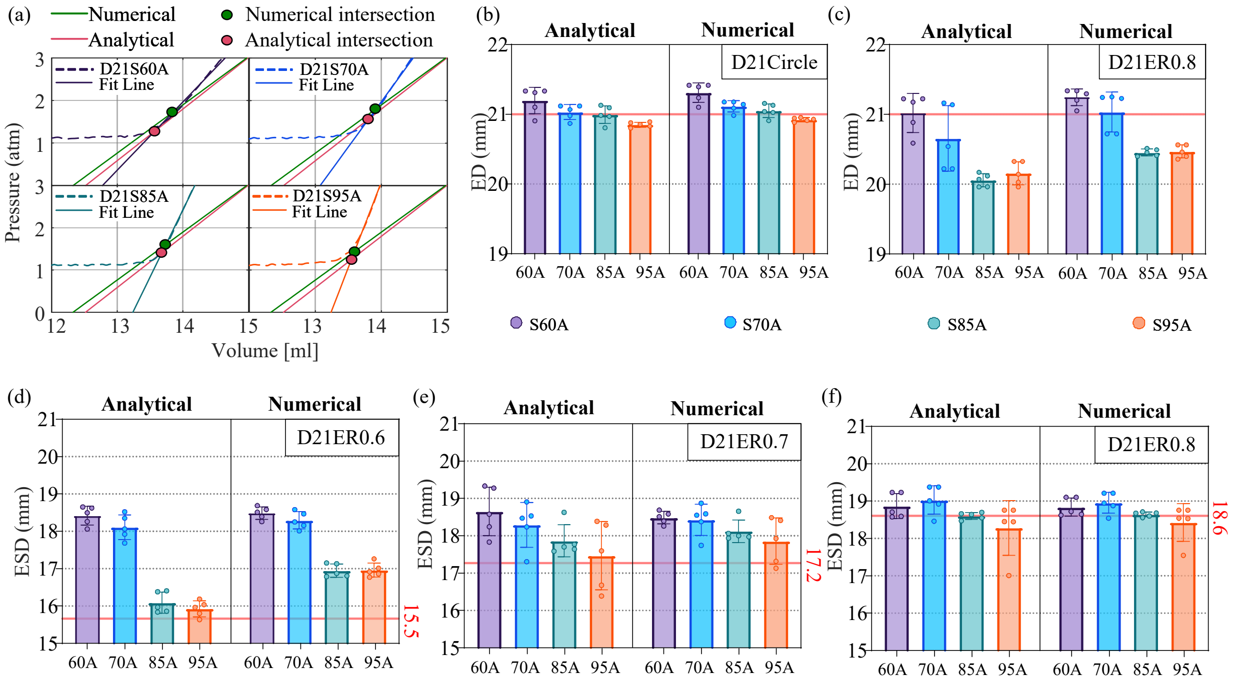

Fig. 7. Estimation results for 21 mm circular phantoms and elliptical phantoms with the same circumference of 0.6, 0.7, and 0.8 ratios. (a) Intersection points of fitting lines with analytical and numerical model lines; (b) Estimated diameter of 21 mm 0.8 ratio elliptical phantoms; (c) Estimated the equivalent diameter of 21 mm circular phantoms; (d)-(f) Estimated short diameter of 0.6, 0.7, and 0.8 ratio elliptical phantoms.

which results in a 3 mm difference with a minor diameter (15.51 mm). While the estimated results for the two stiffer elliptical phantoms show greater accuracy, the error of the estimated diameter via the analytical unfolding model remains below 5%. The most accurate for sizing is the 85A shore hardness phantoms with a 0.8 elliptical ratio (0.021% error). The estimations via the numerical unfolding model result in lower accuracy for the 0.6 and 0.7 elliptical ratios. Sizing for the 0.8 ratio phantoms demonstrates high accuracy for all stiffness levels via both models (maximum error value at 2.26%). Phantoms with 95A show the best estimation results, followed by 85A. The maximum standard deviation for the short diameter estimation of phantoms with the same circumference of a 21 mm diameter circle is ±0.19 mm.

For 22 mm diameter phantoms, the intersection points between two models with the fitting line are shown in Fig. 8(a). The intersections (pink and green points) nearly overlap, and their pressure value decreases with the higher stiffness. The estimated average diameter values are drawn in Fig. 8(b) with five tests and the associated standard deviations. The accuracy for all shore hardness ratings are relatively high with errors lower than 2%: 1.67%, 0.78%, 0.68% and 0.37% for 60A to 95A via analytical model, and 1.69%, 0.74%, 0.59% and 0.28% via numerical model. The average estimated diameter via a analytical model for four stiffness levels is between 22.37 and 22.08 mm. For the numerical model, the average diameter varies between 22.37 and 22.06 mm. The maximum standard deviation for estimating 22 mm diameter circle phantoms is ±0.10 mm.

For sizing the equivalent diameter of 0.8 ratio elliptical phantoms with the same circumference, the value decreases with the increase of the hardness (Fig. 8(c)), and the results of the two models are almost the same. The smallest average estimated value is 22.08 mm for 95A via an analytical model. However, the highest error is still lower than 3% for the 95A level (21.41 mm with 2.69% error by analytical model), and the error decreases with softer phantoms (Fig. 9(c)). The estimated short diameters of 60A phantoms of three elliptical ratios are located between 19 to 20 mm and increase with the ratio. There is about 3 mm difference between the actual short diameter with the estimated value for 0.6 ratio (error of 19.22% and 18.92% for numerical and analytical model) and around 1.5 mm difference for 0.7 ratio (error of 15.04% and 14.68% for numerical and analytical model) (Fig. 8(d) and (e)). The errors for two stiffer phantoms are around 5%, while they are around 10% for two softer phantoms for a 0.7 ratio (Fig. 9(d)). Estimating the short diameter of elliptical phantoms with the same circumference shows the lowest errors at all hardness levels is for a 0.8 elliptical ratio, and the 60A phantom assessed by analytical models results in the maximum error out of the four levels (2.55%), as shown in Fig. 9(c) and (d). With the

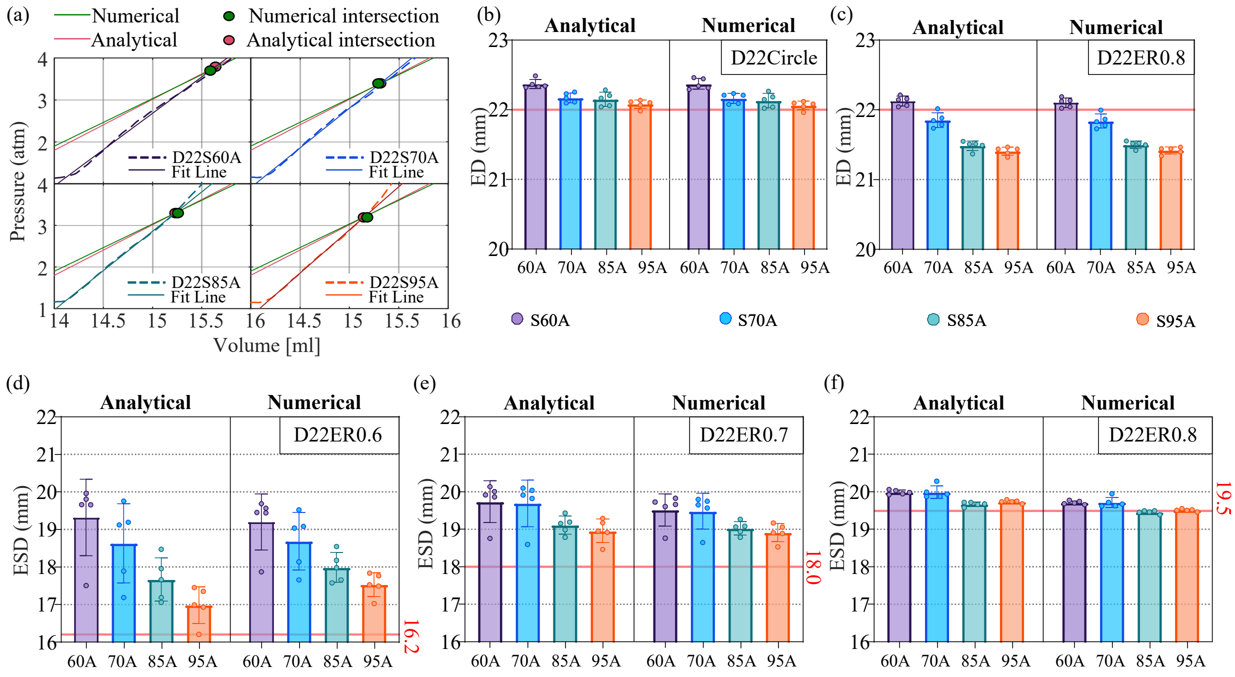

Fig. 8. Estimation results for 22 mm circular phantoms and elliptical phantoms with the same circumference of 0.6, 0.7, and 0.8 ratios. (a) Intersection points of fitting lines with analytical and numerical model lines; (b) Estimated diameter of 22 mm circular phantoms; (c) Estimation of the equivalent diameter of 22 mm 0.8 ratio elliptical phantom; (d)-(f) Estimated short diameter of 0.6, 0.7, and 0.8 ratio elliptical phantoms.

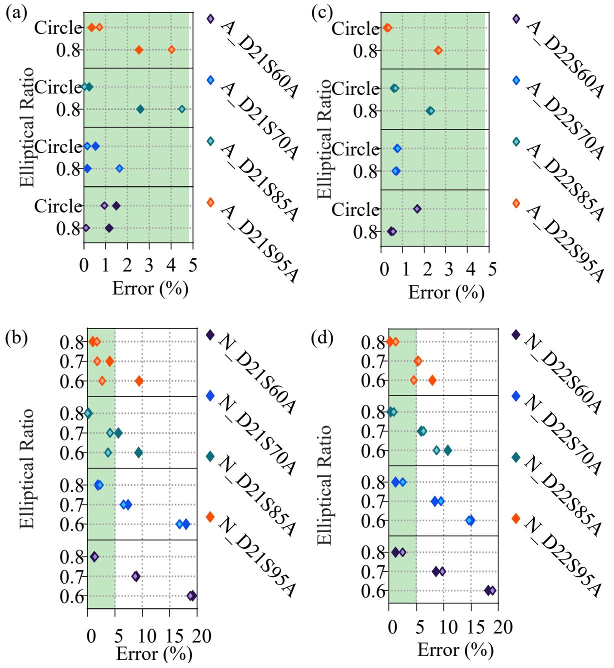

Fig. 9. Estimation error for both analytical and numerical models. (a) Errors of diameter estimation for 21 mm circle and 0.8 ratio elliptical phantoms; (b) Errors of minor diameter estimation for 21 mm elliptical phantoms; (c) Errors of diameter estimation for 22 mm circle and 0.8 ratio elliptical phantoms; (d) Errors of minor diameter estimation for 22 mm elliptical phantoms.

exception of phantoms with a 0.6 elliptical ratio at 85A and 95A, the sizing values via the two models are similar and have relatively small associated standard deviations.

IV. DISCUSSION

An automated inflation device was developed and interfaced with a commercially available BAV balloon catheter to estimate the size and shape of the valve annulus using real-time balloon internal pressure and volume data. The study has indicated that sufficiently accurate and repeatable estimation of annular diameters can be obtained from intra-balloon p-v data. The proposed sizing algorithm has excellent accuracy for circular idealised compliant annular diameter estimation (maximum error 1.69%). In addition, the assessment of the short diameter of the stiffer elliptical annular, such as those with shore hardness 85A and 95A, shows good accuracy and reproducibility via an analytical model, which increases in alignment with the increase of the elliptical ratio. Moreover, when the elliptical annulus has a ratio of 0.8, its equivalent diameter can be evaluated as the circular diameter (21 and 22 mm) of the same circumference, resulting in low error.

Intra-operation aortic annulus sizing by balloon was first introduced by Babaliaros *et al.*, where the annular diameter was defined as bigger, same or smaller than the inflated balloon diameter by comparing the internal pressure when the balloon inflated freely or inside the aortic annulus [22]. Compared with the method used in the current study, Babaliaros *et al.* could not obtain the specific dimension information of the annulus. Balloon sizing with associated supra-aortic angiography was investigated and compared with pre-operation imaging-based sizing by Patsalis *et al.* and Thorani *et al.* [24], [25]. Contrast regurgitation was used to observe leakage and judge whether the balloon size was underestimated and decide the size of implanted prosthetic valve. However, these studies did not consider the elliptical geometry of the aortic annulus. If leakage was observed when the balloon was fully inflated inside a non-circular annulus, the valve size recommended might be overestimated and cause an annular rupture. The short diameter estimated in this study could help in choosing the size of the transcatheter heart valve (THV); as mentioned in [34], the size of implanted devices were associated with the short diameter of the elliptical annulus, and the results showed no transvalvular regurgitation and larger effective orifice area.

In estimating the results via the analytical and numerical models for the circular phantom, the assessed diameter of the 21 mm annulus via numerical model is a little higher than that of the analytical model, and it is almost the same as in the 22 mm annular phantoms. In addition, the slopes of the two model lines are similar, with an RMSE equal to 0.005 (R^2 = 0.995). These indicate that the tapered end geometry and varied thickness of the tapered regions have a small influence on the sizing strategy.

Furthermore, the estimations of the minor diameter for both two sizes of high elliptical soft annular phantoms (0.7 ratio) with a material shore hardness of 60A and 70A have around 3 mm difference from the actual value. The minor pressure increment induced by the soft phantom expansion and caused by balloon inflation may have influenced this inaccuracy. Thus, the peak of the second derivative of the data might not be created at the point when the balloon starts to expand the short axis of the phantom, as shown by the blue and purple lines in Fig. 6(a) and (b). The resulting points than the expansion, resulting in a noticeable increase of the inner pressure of the balloon. In a sample size of 374 patients, the mean non-circular annular ratio was reported as 0.77±0.04 by Maeno *et al.* [29]. Thus, the sizing method with good precision for elliptical annular phantoms (0.7 and 0.8 ratios) demonstrates the ability to size the annulus of patients with symptomatic severe aortic stenosis. Regarding the compliance of the aortic annulus, the average of the calcified annulus was measured as 22.6 MPa, which can be transferred to 84.9A [26], [28]. The phantoms used in this study with shore hardness 85A resulted in the best estimation for 21 mm circular phantoms and elliptical phantoms with a 0.8 annular ratio. They ranked second-best for 22 mm circular phantoms and elliptical phantoms with a 0.7 annular ratio. Therefore, according to these clinically recorded annular characteristics, the sizing approach proposed in this work shows the potential to estimate the calcified annulus.

Based on the pre-operative imaging measurement, 10% oversizing of the prosthesis aortic valve selection is commonly chosen by clinician [35]. However, it is worth noting that the condition of aortic stenosis and the subjective nature of imaging measurements can sometimes lead to the selection of prosthetic valves that are still undersized even when a 10% larger valve is used. This undersizing has been associated with cases of moderate to severe paravalvular regurgitation [36]. Conversely, there is no adjustment required for the intraoperative method mentioned in this paper, thus improving the accuracy of the valve selection.

However, one of the limitations is that the standalone pressure-volume curves of the balloon for sizing may not be sufficient to determine more characteristics of complex aortic annuli. Combining these models with intra-operative imaging could provide additional details of the aortic valve region. In addition, only one size of valvuloplasty balloon catheter was used for testing in this work. To further verify the wider applicability of the sizing method, it is necessary to include more sizes and typologies of commercially available valvuloplasty balloon catheters. Balloon catheters are used to dilate the calcified aortic leaflets, whose height ranges from 12 to 28 mm [37], and the length of left ventricular outflow is about 25 mm [38]. Therefore, some continuity of the leaflets with the basal ring and the left ventricular outflow tract acts as an extension. In this initial study, we have selected a phantom axial length of 40 mm because it is coherent with the anatomical dimensions, and allows to cover the whole effective dilatation area of the balloon, decreasing the influence of the length. The shorter dilatation lengths, which are anatomically possible, could cause some "waist effect", which would affect the accuracy of the diameter estimation. Therefore, future work will need to investigate the influence of the length of the phantom on the balloon sizing approach.

From a technical perspective, the main goal of this work is to propose a new intra-operative aortic annulus balloon sizing method that provides more specific dimension details, as well as information about the compliance and more complex geometry features of the annulus. The underlying application is to enhance the selection of transcatheter valves, minimizing complications caused by suboptimal device sizing. In addition, it is intended as a verification tool to potentially refine the measurements recorded from imaging techniques. To test this sizing method in a more realistic environment, it is suggested that future studies include the actual shape of the aortic root, with sinus and leaflets, and consider the influence of the physiological operating conditions. Furthermore, since the slope of the increment pressure region increases with the rigidity of the phantoms, a strategy to assess the aortic annulus material properties can be implemented with an analytical model considering obvious deformations of the annulus.

V. CONCLUSION

An aortic annulus sizing approach based on the relationship between the internal balloon pressure and volume was developed to estimate the diameter of a circular annulus and the smallest diameter of a non-circular annulus. The approach was then validated via experimental tests. Both analytical and numerical models of the balloon were utilised in the sizing algorithm for dimension assessment. The results confirmed a high accuracy for different compliant circular annular phantoms and good precision for the short diameter estimation of stiffer elliptical phantoms (85A and 95A) or phantoms with a larger annular ratio (0.8). This specific diameter sizing will offer the operator useful supplementary information for THV selection and improve operation outcomes after implantation. In the future, the use of more realistic annular phantoms within a fluid environment and an additional strategy for assessing the material properties of the annulus will be investigated.

REFERENCES

[1] V. T. Nkomo *et al.*, "Burden of valvular heart diseases: a population-based study," *THE LANCET*, vol. 368, no. 9540, pp. 1005–1011, 2006.

[2] M. R. Reynolds *et al.*, "Cost-effectiveness of transcatheter aortic valve replacement with a self-expanding prosthesis versus surgical aortic valve replacement," *Journal of the American College of Cardiology*, vol. 67, no. 1, pp. 29–38, 2016.

[3] B. Iung *et al.*, "Contemporary presentation and management of valvular heart disease: the eurobservational research programme valvular heart disease ii survey," *Circulation*, vol. 140, no. 14, pp. 1156–1169, 2019.

[4] S. Yadgir *et al.*, "Global, regional, and national burden of calcific aortic valve and degenerative mitral valve diseases, 1990–2017," *Circulation*, vol. 141, no. 21, pp. 1670–1680, 2020.

[5] M. B. Leon *et al.*, "Transcatheter aortic-valve implantation for aortic stenosis in patients who cannot undergo surgery," *New England Journal of Medicine*, vol. 363, no. 17, pp. 1597–1607, 2010.

[6] S. Arora *et al.*, "Transcatheter aortic valve replacement: comprehensive review and present status," *Texas Heart Institute Journal*, vol. 44, no. 1, pp. 29–38, 2017.

[7] A. Harky *et al.*, "Stented versus stentless aortic valve replacement in patients with small aortic root: a systematic review and meta-analysis," *Innovations*, vol. 13, no. 6, pp. 404–416, 2018.

[8] A. Cribier *et al.*, "Percutaneous transcatheter implantation of an aortic valve prosthesis for calcific aortic stenosis: first human case description," *Circulation*, vol. 106, no. 24, pp. 3006–3008, 2002.

[9] H. Möllmann *et al.*, "Complications of transcatheter aortic valve implantation (tavi): how to avoid and treat them," *Heart*, vol. 101, no. 11, pp. 900–908, 2015.

[10] M. Scharfschwerdt *et al.*, "Hemodynamics of the edwards sapien xt transcatheter heart valve in noncircular aortic annuli," *The Journal of Thoracic and Cardiovascular Surgery*, vol. 148, no. 1, pp. 126–132, 2014.

[11] C. M. Otto *et al.*, “2020 ACC/AHA guideline for the management of patients with valvular heart disease: executive summary: a report of the american college of cardiology/american heart association joint committee on clinical practice guidelines,” *Journal of the American College of Cardiology*, vol. 77, no. 4, pp. 450–500, 2021.

[12] H. Jilaihawi *et al.*, “Prosthesis-patient mismatch after transcatheter aortic valve implantation with the medtronic-corevalve bioprosthesis,” *European heart journal*, vol. 31, no. 7, pp. 857–864, 2010.

[13] A. Calleja *et al.*, “Automated quantitative 3-dimensional modeling of the aortic valve and root by 3-dimensional transesophageal echocardiography in normals, aortic regurgitation, and aortic stenosis: comparison to computed tomography in normals and clinical implications,” *Circulation: Cardiovascular Imaging*, vol. 6, no. 1, pp. 99–108, 2013.

[14] K. Shahgaldi *et al.*, “Transesophageal echocardiography measurements of aortic annulus diameter using biplane mode in patients undergoing transcatheter aortic valve implantation,” *Cardiovascular ultrasound*, vol. 11, no. 1, pp. 1–7, 2013.

[15] R. K. Binder *et al.*, “The impact of integration of a multidetector computed tomography annulus area sizing algorithm on outcomes of transcatheter aortic valve replacement: a prospective, multicenter, controlled trial,” *Journal of the American College of Cardiology*, vol. 62, no. 5, pp. 431–438, 2013.

[16] K. Otani *et al.*, “Assessment of the aortic root using real-time 3d transesophageal echocardiography,” *Circulation Journal*, vol. 74, no. 12, pp. 2649–2657, 2010.

[17] C. Mahon and R. Mohiaddin, “The emerging applications of cardiovascular magnetic resonance imaging in transcatheter aortic valve implantation,” *Clinical Radiology*, vol. 76, no. 1, pp. 73–e21, 2021.

[18] C. Mork *et al.*, “Aortic annular sizing using novel software in three-dimensional transesophageal echocardiography for transcatheter aortic valve replacement: A systematic review and meta-analysis,” *Diagnostics*, vol. 11, no. 5, p. 751, 2021.

[19] T. Rogers and R. Waksman, “Role of cmr in tavr,” *JACC: Cardiovascular Imaging*, vol. 9, no. 5, pp. 593–602, 2016.

[20] A. M. Kasel *et al.*, “Standardized imaging for aortic annular sizing: implications for transcatheter valve selection,” *JACC: Cardiovascular Imaging*, vol. 6, no. 2, pp. 249–262, 2013.

[21] T. Jurencak *et al.*, “Mdct evaluation of aortic root and aortic valve prior to tavi. what is the optimal imaging time point in the cardiac cycle?” *European radiology*, vol. 25, no. 7, pp. 1975–1983, 2015.

[22] V. C. Babaliaros *et al.*, “Use of balloon aortic valvuloplasty to size the aortic annulus before implantation of a balloon-expandable transcatheter heart valve,” *JACC: Cardiovascular Interventions*, vol. 3, no. 1, pp. 114–118, 2010.

[23] A. G. Cerillo *et al.*, “Sizing the annulus for transcatheter aortic valve implantation: more than a simple measure?” *European Journal of Cardio-Thoracic Surgery*, vol. 41, no. 3, pp. 717–718, 2012.

[24] P. C. Patsalis *et al.*, “Preparatory balloon aortic valvuloplasty during transcatheter aortic valve implantation for improved valve sizing,” *JACC: Cardiovascular Interventions*, vol. 6, no. 9, pp. 965–971, 2013.

[25] V. H. Thourani *et al.*, “Balloon versus computed tomography sizing of the aortic annulus for transcatheter aortic valve replacement and the impact of left ventricular outflow tract calcification and morphology on sizing,” *J invasive Cardiol*, vol. 27, no. 7, pp. 295–304, 2016.

[26] A. Hamdan *et al.*, “Deformation dynamics and mechanical properties of the aortic annulus by 4-dimensional computed tomography: insights into the functional anatomy of the aortic valve complex and implications for transcatheter aortic valve therapy,” *Journal of the American College of Cardiology*, vol. 59, no. 2, pp. 119–127, 2012.

[27] H. Qi *et al.*, “Durometer hardness and the stress-strain behavior of elastomeric materials,” *Rubber chemistry and technology*, vol. 76, no. 2, pp. 419–435, 2003.

[28] D. Guarnera *et al.*, “Mechanical characterization of 3d printed mimic of human artery affected by atherosclerotic plaque through numerical and experimental methods,” *Biomechanics and Modeling in Mechanobiology*, vol. 20, no. 5, pp. 1969–1980, 2021.

[29] Y. Maeno *et al.*, “Transcatheter aortic valve replacement with different valve types in elliptic aortic annuli,” *Circulation Journal*, pp. CJ–16, 2017.

[30] P. Blanke *et al.*, “Ct in transcatheter aortic valve replacement,” *Radiology*, vol. 269, no. 3, pp. 650–69, 12 2013.

[31] A. Papachristidis *et al.*, “Three-dimensional measurement of aortic annulus dimensions using area or circumference for transcatheter aortic valve replacement valve sizing: does it make a difference?” *Journal of the American Society of Echocardiography*, vol. 30, no. 9, pp. 871–878, 2017.

[32] D. Liang *et al.*, “Finite element analysis of the implantation of a balloon-expandable stent in a stenosed artery,” *International journal of cardiology*, vol. 104, no. 3, pp. 314–318, 2005.

[33] F. Sturla *et al.*, “Impact of different aortic valve calcification patterns on the outcome of transcatheter aortic valve implantation: A finite element study,” *Journal of Biomechanics*, vol. 49, no. 12, pp. 2520–2530, 2016.

[34] E. Salaun *et al.*, “Effect of oversizing and elliptical shape of aortic annulus on transcatheter valve hemodynamics: An in vitro study,” *International journal of cardiology*, vol. 208, pp. 28–35, 2016.

[35] T. Walther *et al.*, “Transapical aortic valve implantation: Step by step,” *The Annals of Thoracic Surgery*, vol. 87, no. 1, pp. 276–283, 2009.

[36] T. Okuno *et al.*, “Heart valve sizing and clinical outcomes in patients undergoing transcatheter aortic valve implantation,” *Catheterization and cardiovascular interventions*, vol. 98, no. 5, pp. E768–E779, 2021.

[37] H.-J. Schäfers *et al.*, “Cusp height in aortic valves,” *The Journal of Thoracic and Cardiovascular Surgery*, vol. 146, no. 2, pp. 269–274, 2013.

[38] R. Walmsley, “Anatomy of left ventricular outflow tract,” *British heart journal*, vol. 41, no. 3, pp. 263–7, 3 1979.